

Influence of Sample Height-to-Width Ratios on Failure Mode for Rectangular Prism Samples of Hard Rock Loaded In Uniaxial Compression

Diyuan Li · Charlie C. Li · Xibing Li

Received: 26 December 2009 / Accepted: 15 November 2010 / Published online: 4 December 2010
© The Author(s) 2010. This article is published with open access at Springerlink.com

Abstract Surface-parallel slabbing is a failure mode often observed in highly stressed hard rocks in underground excavations. This paper presents the results of experimental studies on slabbing failure of hard rock with different sample height-to-width ratios. The main purpose of this study was to find out the condition to create slabbing failure under uniaxial compression and to determine the slabbing strength of hard rock in the laboratory. Uniaxial compression tests were carried out using five groups of granite specimens. The mechanical parameters of the sample rock, Iddefjord granite from Norway, were measured on the cylindrical and Brazilian disc specimens. The transition of the failure mode was studied using rectangular prism specimens. The initiation and the propagation of slabbing fractures in specimens were identified by examining the relationship among the applied stress, strain and the acoustic emission. The stress thresholds identified were compared to those reported by other authors for crack initiation and brittle failure. It is observed that the macro failure mode will be transformed from shear to slabbing when the height/width ratio is reduced to 0.5 in the prism specimens under uniaxial compression. Micro σ_1 -parallel fractures initiate when the lateral strain departs from its linearity. Slabbing fractures are approximately parallel to the loading direction. Laboratory tests show that the slabbing strength (σ_{sl}) of hard rock is about 60% of its uniaxial compression strength. It means that if the maximum

tangential stress surrounding an underground excavation reaches about the slabbing threshold, slabbing fractures may take place on the boundary of the excavation. Therefore, the best way to stop or eliminate slabbing failure is to control the excavation boundary to avoid the big stress concentration, so that the maximum tangential stress could be under the slabbing threshold.

Keywords Failure mode · Shear failure · Slabbing · Spalling · Extension strain · Acoustic emission · Sample height-to-width ratio · Hard rock

1 Introduction

With increasing depths of mining and tunneling projects, it has been observed that at high stresses hard rocks fail more often in slabbing (or spalling) rather than in shear. Spalling refers to a failure process involving extensional splitting cracks (Fairhurst and Cook 1966). According to Ortlepp's description (Ortlepp 1997), spalling or slabbing is generally defined as the formation of stress-induced slabs on the boundary of an underground excavation. It initiates in the region of maximum tangential stresses and results in a V-shaped notch that is local to the boundary of the opening. This type of failure is typical in strain burst of hard rocks (Ortlepp 2001). Besides, on the boundary of underground openings, slabbing is also observed in hard rock pillars (Exadaktylos and Tsoutrelis 1995; Martin and Maybee 2000). For example, Martin and Maybee (2000) observed that the dominant failure mode was progressive slabbing and spalling in pillars of some Canadian hard rock mines. It shows that the strength of hard rock pillar is directly related to the pillar width-to-height ratio and pillar failure is seldom observed in pillars where the width-to-height ratio is greater

D. Li (✉) · X. Li
School of Resources and Safety Engineering, Central South University, Changsha 410083, Hunan, China
e-mail: lidiyuan123@hotmail.com

C. C. Li
Department of Geology and Mineral Resources Engineering,
The Norwegian University of Science and Technology (NTNU),
7491 Trondheim, Norway

than 2. However, the failure of pillars is different from the failure of laboratory samples. At first, pillar failure is related to the strength of rock masses, but sample failure is related to the strength of intact rock. Second, the strength of hard rock pillars is lower than the uniaxial compression strength [accounting for about $(60 \pm 10)\%$ of σ_c], irrespective of the width-to-height ratio of the pillars. Third, size and end effects influence the failure mode of laboratory samples and mining pillars in different ways to some degree. Martin and Maybee also indicated the influence of the confining stress in short pillars. Because at pillar $W/H > 2$ the confinement at the core of the pillar increases significantly, the use of Hoek–Brown brittle parameters will be less appropriate. Hence, the empirical pillar strength formulas should be limited to pillar $W/H < 2$ (namely $H/W > 0.5$). Recently, the spalling failure of hard rock specimens was numerically modeled by Cai (2008) using FEM/DEM combined numerical tool (ELFEN). It shows that the generation of tunnel surface-parallel fractures and microcracks is attributed to material heterogeneity and the existence of relatively high intermediate principal stress (σ_2), as well as zero to low minimum principal stress (σ_3) confinement. At present, the International Society for Rock Mechanics (ISRM) has appointed a commission on rock spalling (<http://www.isrm.net/gca/index.php?id=900>) among its eight commissions. The commission is supposed to put forward some suggestions on laboratory procedures required to assess crack initiation (CI) in laboratory tests using strain gauges, LVDTs and AE, and to suggest what to do if only UCS is available and so on. It can be seen that the problem of spalling and slabbing failure has become a new challenge in rock mechanics.

Figure 1 shows a photograph of slabbing failure in a 3-year-old mine drift excavated in quartzite at 1,000 m depth. The roof was exposed when another parallel drift was excavated. The slabbing failure, in many cases, is shown as densely spaced “onion-skin” fractures or slabs in highly stressed rocks after excavation. The spacing of the stress-induced fractures depends on the magnitude of rock stresses and the strength of rock, as well as the material heterogeneity (Cai 2008). On the one hand, the present studies on slabbing failure of hard rocks mainly concentrate on the description of slabbing phenomenon and how to control slabbing failure in situ (Dowding and Andersson 1986; Fang and Harrison 2002; Martin et al. 1997). On the other hand, most studies are concerned with shear failure of hard rock (Bieniawski 1967a, b, c; Brady and Brown 2004; Lockner et al. 1991; Mogi 2007; Moore and Lockner 1995; Savage et al. 1996) except for a few studies on splitting failure (Holzhausen and Johnson 1979; Horii and Nemat-Nasser 1986; Li Chunlin 1995; Wong et al. 2006) in the laboratory compression tests.



Fig. 1 Slabbing failure in the roof of a 3-year-old mine drift excavated in quartzite at 1,000 m depth. The roof was exposed when another parallel drift was excavated

Both the classic Mohr–Coulomb criterion and the empirical Hoek–Brown criterion are essentially for the shear failure of rock. These criteria are suitable when the confinement pressure is big enough to create shear failure. Under uniaxial compression, both shear failure criteria cannot be applied when the failure is splitting (a kind of extension failure). Stacey (1981) proposed a simple extension strain criterion for fracture of brittle rock. He points out that when the total extension strain in the rock exceeds a critical value, the extension fracture of brittle rock will initiate. However, the critical value of extension strain of brittle rock is difficult to find out. The criterion is not widely used in engineering even though the formula is very simple.

To better understand the failure process before peak strength in hard rock, Eberhardt (1998), Eberhardt et al. (1998, 1999) did a number of experiments to identify and characterize the brittle fracture process by uniaxial compression testing of pink Lac du Bonnet granite in Canada. The shape of the specimens is cylindrical and the height-to-diameter ratio is approximately 2.25. The crack closure (σ_{cc}), crack initiation (σ_{ci}), crack damage (σ_{cd}) and peak strength (σ_{UCS}) in the stress–strain curves were identified by strain gauges and acoustic emission (AE) techniques. However, the failure mode of hard rock under confinement, the end effect and the size effect in the specimens have not been discussed in those studies. The compression failure of concrete columns and the size effect on compression strength of a columns have been carefully studied by Bazant et al. (Bazant et al. 1999; Bazant and Xiang 1996; Bazant and Xiang 1997). It is well known that the compression strength of a

column will change from material strength (σ_{UCS}) to buckling strength when the slenderless is increasing to a critical value. The question is what will happen if the slenderless of rock or concrete column is reduced to a certain small value. Will the failure mode change in the short samples?

The brittle failure of hard rock under compression has been studied extensively since the 1960s, for instance by Cook (1965), Bieniawski (1967a, b, c), Ewy and Cook (1990a, b), Li and Nordlund (1993), Martin and Chandler (1994), Hajiabdomajid et al. (2002), Wong et al. (2006) and Cai (2008). The methodologies of the studies involve laboratory study, numerical modeling, macroscopic and microscopic observations, site investigation and mathematic deduction. In all the studies, the stress–strain constitutive law and the failure mode of the rock are the most concerning issues. With increasing excavation depth, it has been observed that some fractures are developed parallel to the excavation periphery in hard rock masses (Germanovich and Dyskin 2000; Kaiser and McCreath 1994; Martin et al. 1997; Ortlepp 1997; Ortlepp and Stacey 1994). The slabbing fractures parallel to the excavation periphery in deep underground openings have been studied by some engineers and scholars. For instance, Diederichs (2002, 2007), Diederichs et al. (2004) has paid much attention to the tensile spalling failure of hard rock. He compared two curves between the long-term strength of laboratory samples and the in situ strength of hard rock. He concluded that the in situ strength of hard rock was less than the long-term strength of laboratory samples when the confining stress was relatively low compared with UCS, and spalling/slabbing failure might occur at this confining stress condition.

Based on the site observations, we tried to design some laboratory tests to find out the mechanism of slabbing failure and to determine the slabbing strength of hard rock. However, so far, research on this subject is very limited. The objectives of this paper are to investigate the influence of sample height-to-width ratio for the transition of failure mode from shear to slabbing and to determine the slabbing strength of hard rock by laboratory tests. Five groups of laboratory tests were carried out, which include cylinder tests, Brazilian tests and three groups of prism specimens' tests. The mechanical parameters of the sample rock, Iddefjord granite from Norway, were measured on the cylindrical specimens and the disc specimens. The transition of the failure mode was studied using the rectangular prism specimens. AE was monitored during testing to detect the crack initiation and propagation in the samples. Both axial and lateral strains were logged in the tests, so that the stress–strain curves could be obtained.

2 Experimental Tests

2.1 Specimens

Five groups of specimens from granite blocks taken from a quarry in Iddefjord, Norway, were prepared in the laboratory. The average density of the granite is $2,620 \text{ kg/m}^3$. The P -wave velocity ranges from 4,000 to 4,700 m/s. Seah (2006) has done some laboratory tests on Iddefjord granite. The physical and mechanical properties of the rock can also be found in his Ph.D. thesis. The five groups of specimens are:

- Group A: three cylindrical specimens, 50 mm in diameter and 125 mm in length;
- Group B: three Brazilian disc specimens, 50 mm in diameter and 25 mm in thickness;
- Group C: three prism specimens, $50 \times 25 \times 120 \text{ mm}$, with a height/width ratio of 2.4;
- Group D: three prism specimens, $50 \times 25 \times 50 \text{ mm}$, with a height/width ratio of 1.0;
- Group E: three prism specimens, $50 \times 25 \times 25 \text{ mm}$, with a height/width ratio of 0.5.

Groups A and B were used to determine the uniaxial compressive strength (UCS) and indirect tensile strength of the granite. Groups C, D and E were used to investigate the influence of the height/width ratio to the transition of the failure mode. The geometric shapes of the five groups of specimens are shown in Fig. 2. The loading ends of all the cylindrical and prismatic specimens were ground parallel and smooth to minimize the end effects. Axial and lateral strain gauges were mounted on the cylindrical surface for the cylindrical specimens and on both the front and back sides of the prismatic specimens to measure the axial and lateral strain during testing.

2.2 Equipments and Testing Procedures

The experiments were carried out on two hydraulic servo-controlled machines, Instron 1346 and Instron 1342, in the Mechanical Testing Centre of Central South University, China. The testing system is controlled by computer and the load and deformation data can be acquired automatically. The uniaxial compression tests of Groups A, C, D and E were carried out on Instron 1346, which has a load capacity of 2,000 KN. The Brazilian tests of Group B were undertaken on Instron 1342, which has a load capacity of 250 KN. The machines are shown in Fig. 3. The specimen's ends were directly in contact with the machine except that a little lubricant was present on the interface under testing.

An AE detecting sensor, a PCI-2 AE data-collecting system and a DH-3817 dynamic-static strain acquisition

Fig. 2 The geometric shapes of the five groups of Iddefjord granite specimens (H , W , T represent height, width and thickness of the prism specimen, respectively)

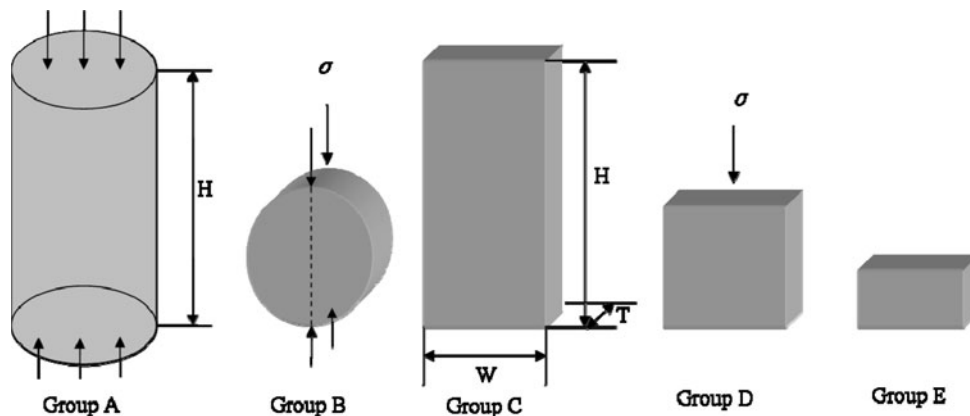


Fig. 3 The stiff test machines Instron 1342 and 1346 at Central South University



system were also used for the tests. The threshold of AE trigger level was set to 42 dB for each specimen except A1. The AE signals measured in the sensors were amplified by the gain of 40 dB with pre-amplifiers. The data acquisition rate was set to 0.5 MHz, and a waveform could be measured for every 2 μ s. It should be noted that the threshold of AE trigger level in specimen A1 is 39 dB, and it can be seen that the AE counts rate curve oscillates more seriously than A2 and A3 at the beginning of the compression stage because of the influence of background noise. Therefore, the threshold value was set to 42 dB for the other specimens after testing A1. There are two cross-strain gauges on each specimen to measure the axial and lateral strain.

Uniaxial compression tests of group A and Brazilian tests of group B were first conducted to obtain the basic mechanical properties of the Iddefjord granite. The prism specimens in groups C, D and E were uniaxially loaded under compression to study the transition of the failure mode. To study and observe the failure process of the specimens, AE events were monitored and photos of the testing specimens were taken in the process of loading. The loading rate was controlled at 60 KN/min in the beginning

stage. When the load reached about 150 KN, the loading was changed from load control to displacement control at a rate of 0.1 mm/min.

2.3 Damage Thresholds

It is believed that some stress thresholds exist during the brittle fracturing on the progressive degradation of intact rock under compression. To identify these crack initiation and propagation thresholds in brittle rock, some scholars (Diederichs et al. 2004; Eberhardt et al. 1998) have made contributions to this research field based on axial and lateral deformation measurements, and AE records during laboratory tests. According to the stress–strain characteristics displayed by the axial and lateral strain measurements and AE count rate curves, three damage thresholds were identified during the tests in this paper. By analyzing the laboratory testing data, the axial stress–strain curve, the lateral stress–strain curve, and the logarithmic AE count rate–strain curve can be obtained in a typical figure. Therefore, we define the three damage threshold values in the stress–strain curves for the long specimens in Group A and Group C as follows:

- Stable crack initiation stress (σ_{st} , Point P): the threshold at which the corresponding logarithmic AE count rate curve begins to monotonically increase after oscillating in the beginning stage. It means that the crack growth can be stopped by controlling the applied load.
- Unstable crack development stress (σ_{ust} , Point Q): the threshold at which the corresponding logarithmic AE count rate curve begins to abruptly increase prior to failure. It means that the crack growth would continue even if the applied load were kept constant.
- Slabbing crack initiation stress (σ_{sl} , Point M): the threshold at which the lateral stress–strain response is observed to become nonlinear. It means that the extension slabbing fractures initiate in the brittle rock, and nonlinear increasing of lateral extension strain may contribute to slabbing failure.

2.4 Testing Results

2.4.1 Cylinder Compression Tests and Brazilian Disc Tests

Properties of the rock were obtained from the tests of Groups A and B. The properties include the uniaxial compressive strength (σ_c), tensile strength (σ_t), internal friction angle (ϕ), cohesion (c), Young’s modulus (E), Poisson’s ratio (ν), density (γ) and P -wave velocity (V_p), which are listed in Table 1. The values of ϕ , and c are obtained by back-calculations from the fracture angle θ and σ_c by using relationships $\phi = 2\theta - 90^\circ$ and $c = \sigma_c (1 - \sin \phi) / 2 \cos \phi$.

The stress–strain curves of the cylindrical specimens in Group A are shown in Fig. 4, and also the curves of the AE count rate (AE counts per second) to the axial strain are shown in a logarithmic scale in the figures. Specimen A1’s stress–strain curves in Fig. 4a show, for example, that the Iddefjord granite is very brittle and has a uniaxial compressive strength of 197 MPa. The maximum axial strain is about 3,600 $\mu\epsilon$ and the maximum lateral extension strain is about 1,800 $\mu\epsilon$. In the axial stress–strain curve, an initial non-linear behavior owing to crack closure is followed by a linear deformation until the axial stress is about 180 MPa. The lateral strain departs from its linearity when the axial stress is beyond about 130 MPa (point M). After oscillating somehow in the beginning stage of loading, the AE count

rate monotonously increases from stress level of 70–180 MPa (zone PQ in the stress–strain curve) and then abruptly increases prior to failure. Similar phenomena can be seen in specimens A2 and A3, as shown in Fig. 4b, c. Figure 5 shows the macro failure fractures of specimens in Group A after testing. All the specimens in Group A failed in shear from the macro point of view.

Brazilian disc tests of group B were conducted on Instron 1342. The extension strain and the AE counts were monitored during the tests. The extension strain and the AE counts versus time are shown in Fig. 6. The tensile strength

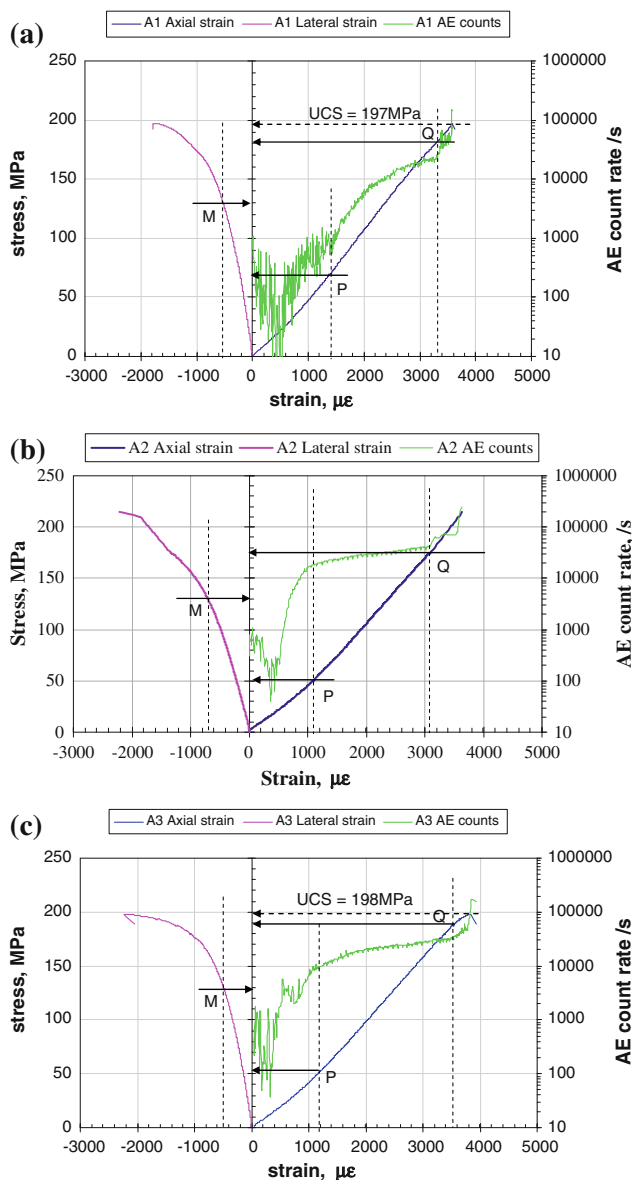


Fig. 4 The stress–strain curves and the AE count rate curves for the cylindrical specimens in group A. **a** Specimen: A1, **b** specimen: A2, **c** specimen: A3

Table 1 Basic mechanical properties (mean values) of the Iddefjord granite

σ_c (MPa)	σ_t (MPa)	σ_c/σ_t	θ	ϕ	c (MPa)	E (GPa)	ν	γ (kg/m ³)	V_p (m/s)
203.3	8.3	24.5	68°	48°	39.0	51.7	0.19	2620	4,550

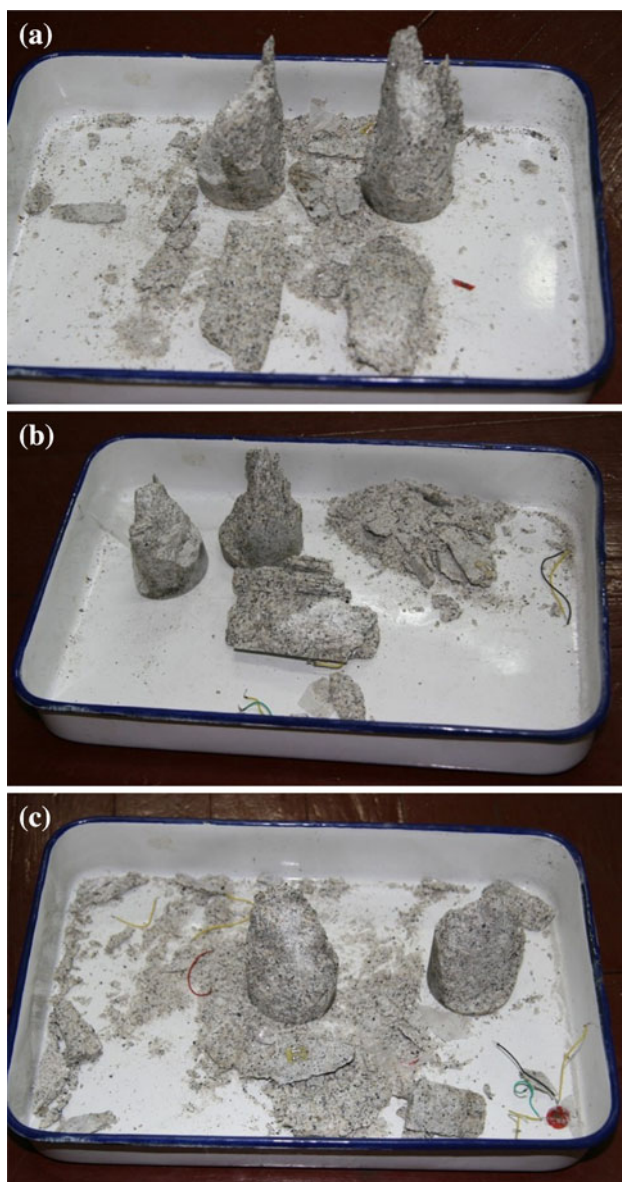


Fig. 5 The macro failure fractures of specimens in Group A after testing. **a** Specimen: A1, **b** specimen: A2, **c** specimen: A3

of specimens B1, B2 and B3 are 9.7, 8.7 and 6.3 MPa, respectively. Their maximum extension strains are 510, 410 and 140 $\mu\epsilon$, respectively. The low value of the extension strain for B3 may be due to the lateral strain gauge attached to the specimen not perpendicular to the loading direction. Sporadic AE events occurred until the load was close to the failure point. For instance, it can be seen that intensive AE occurred prior to failure for the specimen B2 in Fig. 6. A similar phenomenon has been observed in specimens B1 and B3. Figure 7 shows the splitting fractures of the three Brazilian disc specimens after testing. The fracture plane of the specimens is approximately along the loading line.

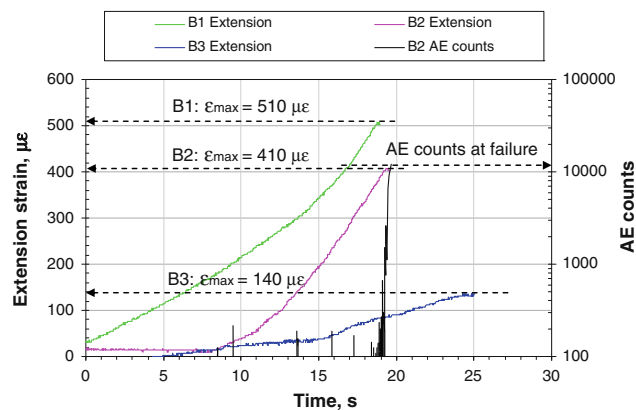


Fig. 6 The extension strain versus time for the Brazilian specimens in Group B and a typical AE counts–time curve for specimen B2

2.4.2 Compression Tests on the Rectangular Prism Specimens

Uniaxial compression tests on the rectangular prism specimens of groups C, D and E were carried out on Instron 1346. The test results of groups C, D and E are summarized in Table 2.

The stress–strain curves and also the logarithmic curves of AE count rate for the specimens in groups C, D and E are shown in Figs. 8, 9 and 10, respectively. For the C specimens ($H/W = 2.4$) in Fig. 8, the average UCS is about 180 MPa, which is about 10% smaller than the UCS of the cylindrical specimens in group A. Both the stress–strain curves and the AE count rate curve are similar to the specimens in group A. The maximum lateral strain of specimen C1 is only about 1,200 $\mu\epsilon$ at failure, but for specimens C2 and C3 it is about 2,000 $\mu\epsilon$. The AE count rate of C2 is quite low at low load levels compared to specimens C1 and C3. However, the AE count rate suddenly increases when the load approaches the ultimate failure level. The typical points (point P, Q and M) on the stress–strain curves can be still recognized in the specimens of group C.

Figure 9 shows the testing results of the specimens in group D ($H/W = 1.0$). Note that the average UCS of the three specimens is about 220 MPa, which is 10% more than the UCS of the cylindrical specimens in group A. Taking specimen D1 as an example in Fig. 9a, a nonlinearity exists in the start portion of the axial stress–strain curve and then it becomes linearly elastic until the stress reaches about 220 MPa. The maximum axial strain is about 3,600 $\mu\epsilon$, but the maximum lateral strain is only 800 $\mu\epsilon$. It means that the lateral deformation of D specimens is confined. The lateral stress–strain curve is almost linear even until the final failure. The AE count rate fluctuates when the axial strain is smaller than 1,400 $\mu\epsilon$ and then it monotonically increases until the axial strain reaches about

Fig. 7 Splitting fractures of the Brazilian disc specimens in group B after testing



Table 2 Testing results of the prism specimens in Groups C, D and E

Specimen number	Height, H (mm)	Width, W (mm)	Thickness, T (mm)	Load, P_{\max} (KN)	UCS, σ_c (MPa)	Young's modulus, E (Gpa)	Poisson's ratio, ν	Fracture angle, θ	Failure mode
C1	120.80	52.20	26.50	236.5	171.0	56.8	0.21	69°	Shear
C2	120.00	51.50	27.60	265.5	186.8	52.7	0.27	70°	Shear
C3	120.70	51.90	26.95	267.0	191.0	50.4	0.19	72°	Shear
D1	51.30	51.90	26.70	320.0	231.0	72.2	0.19	80°	Shear
D2	51.30	51.90	26.70	261.4	188.7	61.6	–	77°	Shear
D3	51.25	51.90	26.70	306.9	221.5	65.4	0.17	78°	Shear
E1	26.40	52.35	26.45	255.1	184.2	57.6	–	85°	Slabbing
E2	26.40	52.35	26.40	315.6	228.4	62.8	0.12	84°	Hybrid
E3	26.40	52.30	26.45	175.7	127.0	40.1	0.18	88°	Slabbing

UCS uniaxial compressive strength

3,000 $\mu\epsilon$. After that it becomes nonlinear and an accelerated increase in AE prior to failure is observed. Similar phenomena occur in specimens D2 and D3, as shown in Fig. 9b, c, except that specimen D2 has a relatively larger AE count rate than specimen D1. It may result from the environmental noises during this test.

Figure 10 shows the testing results of the specimens in group E ($H/W = 0.5$). It seems that these results are much more different than those from the specimens in groups C and D. For example, the UCS of the specimen E1 is about 180 MPa, but it is seen that the axial strain departs from its linearity when the stress reaches about 110 MPa. At this stress level, the AE count rate increases suddenly. The lateral strain of the specimen E1 is disturbed and not listed in Fig. 10a. The curves of specimen E3 (Fig. 10c) are similar to specimens E1. The UCS of the specimen E3 is only 127 MPa. The axial stress–strain curve of specimen E3 also departs from its linearity when the stress reaches about 110 MPa, and at this stress level the AE count rate increases greatly. The strain gauges may become damaged at this load level when slabbing fractures develop. The corresponding lateral strain at this point is about 520 $\mu\epsilon$,

which is almost equal to the maximum extension strain from the Brazilian tests in group B. The UCS of specimen E2 is about 220 MPa. The stress–strain curves of E2 are almost linear prior to failure. The curves of specimen E2 (Fig. 10b) are different from specimens E1 and E3, but similar to the D specimens. The behavior of specimen E2 is considered as an exception from group E, possibly because of the end effects and stress concentration at the corner of the specimen. It can be seen that the failure mode of E2 is different from E1 and E3.

To explain the failure process of specimen E1 and E3 more clearly, the AE counts–time curve and the stress–time curve are shown in Fig. 11. It includes the information of AE counts and applied stress varied with the testing time. Taking the specimen E1 as an example in Fig. 11a, it can be seen that the AE counts increase a lot when the applied stress reaches about 110 MPa. The increase of AE counts during the stress level from 110 to 160 MPa may indicate the initiation and propagation of slabbing fractures in the specimen. Since the fractures are parallel to the maximum loading direction, the specimen can still sustain further stress. It can be found that the slabbing fractures occurred

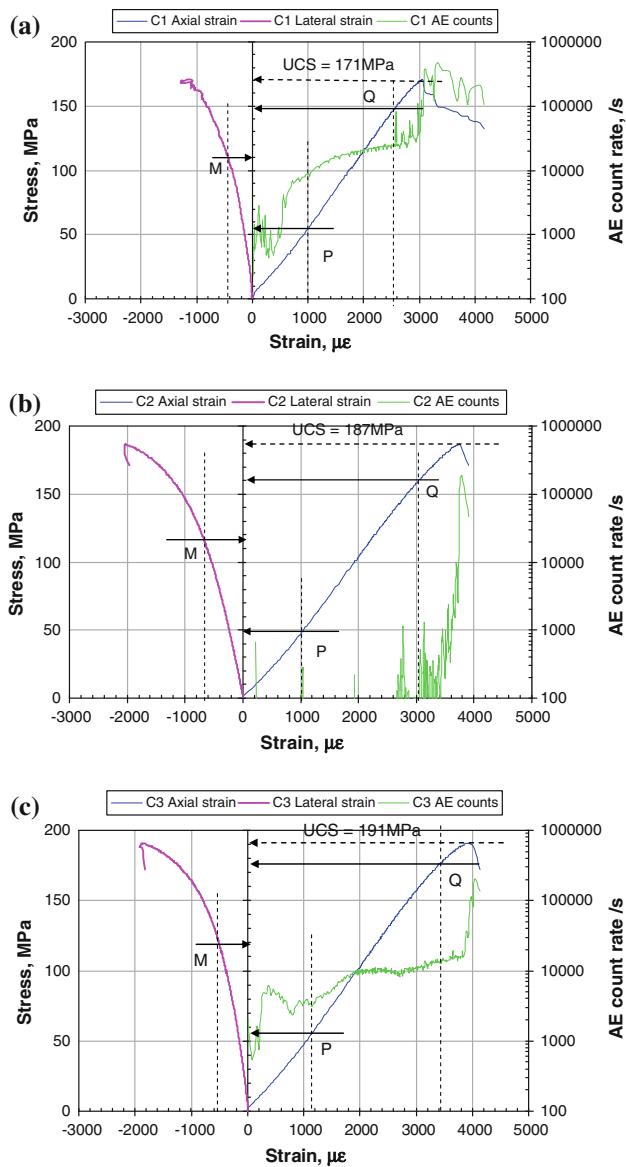


Fig. 8 The stress–strain curves and the AE count rate curves for the prism specimens in group C. **a** Specimen: C1, $\sigma_c = 171$ MPa; **b** specimen: C2, $\sigma_c = 187$ MPa; **c** specimen: C3, $\sigma_c = 191$ MPa

in the specimen E1 from the final failure mode. Similar phenomena can be also observed in the specimen E3. It can be inferred that the slabbing fractures start to propagate at the stress level of 110–120 MPa. From the viewpoint of AE counts curve, the specimen E2 is also an exception in Group E. The reason may be attributed to the confining pressure due to the end effects, which limit the initiation of extension slabbing fractures in the specimen E2. Therefore, we take specimen E2 as an exception in Group E.

Figure 12 shows the failure modes of all the specimens in Groups C, D and E after testing. The failure mode of the specimens in groups C and D is dominant in shear by observing the final macro fractures. However, some splitting fractures and exfoliation failure occurred in the

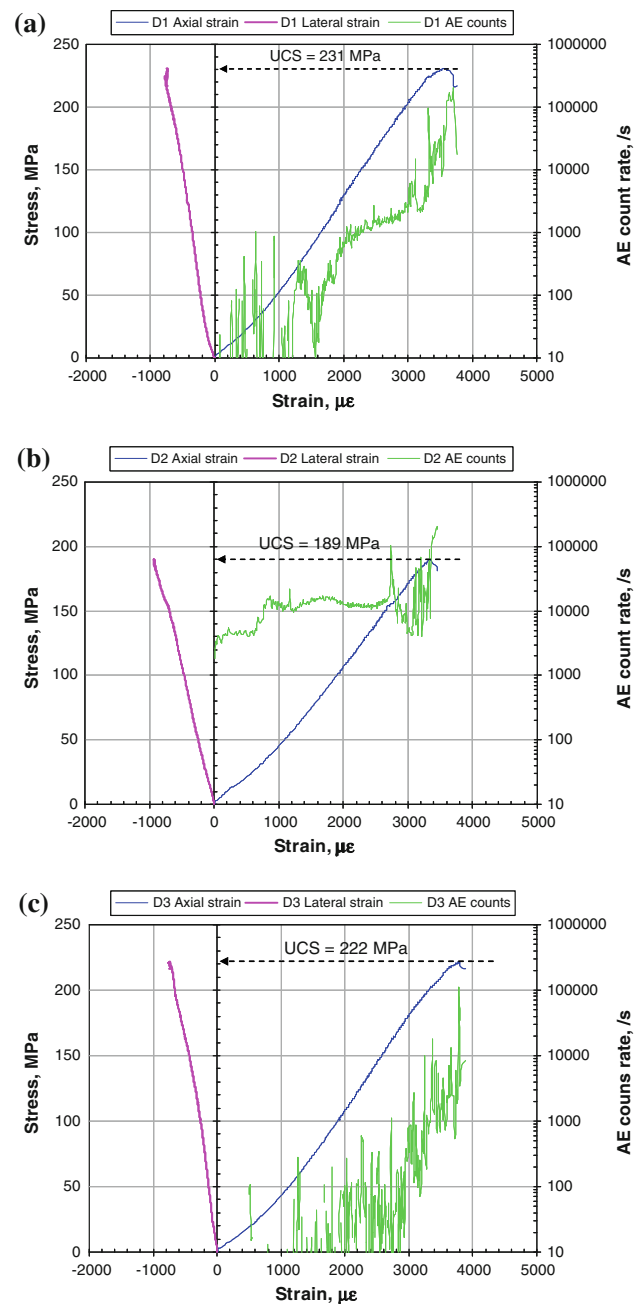


Fig. 9 The stress–strain curves and the AE count rate curves for the prism specimens in group D. **a** Specimen: D1, $\sigma_c = 231$ MPa; **b** specimen: D2, $\sigma_c = 189$ MPa; **c** specimen: D3, $\sigma_c = 222$ MPa

specimens of groups C and D. For the specimens in group E, which are the shortest among the three groups of prismatic specimens, the fracture is approximately vertical, parallel to the direction of loading force. Specimens E1 and E3 failed in a slabbing manner, as seen in Fig. 12g, i. The slabs are thin and are of approximately equal thickness. The slabbing fractures can form either in the long side or in the short side of the sample. It may be dependant on the heterogeneity of the rock samples. Specimen E2 failed at one end, possibly due to stress concentration on the contact surface.

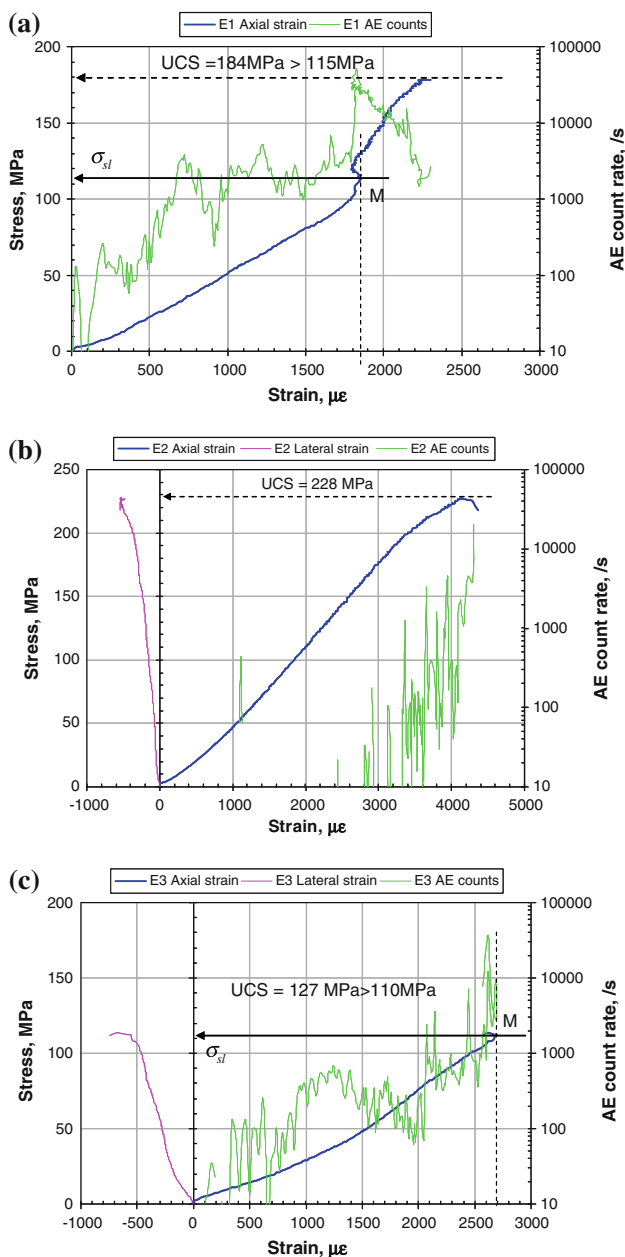


Fig. 10 The stress–strain curves and the AE count rate curves for the prism specimens in group E (σ_{sl} refers to the slabbing strength of the rock). **a** Specimen: E1, $\sigma_c = 184$ MPa, $\sigma_{sl} = 115$ MPa; **b** specimen: E2, $\sigma_c = 228$ MPa; **c** specimen: E3, $\sigma_c = 127$ MPa, $\sigma_{sl} = 110$ MPa

3 Discussion

3.1 The Uniaxial Compressive Strength and the Fracture Angle

The uniaxial compressive strengths (UCS) of all the prismatic specimens (except for specimen E2) in the laboratory tests are plotted versus the H/W ratio in Fig. 13. It is seen that the UCS increases slightly when the H/W ratio decreases from 2.4 (group C) to 1.0 (group D). Shear

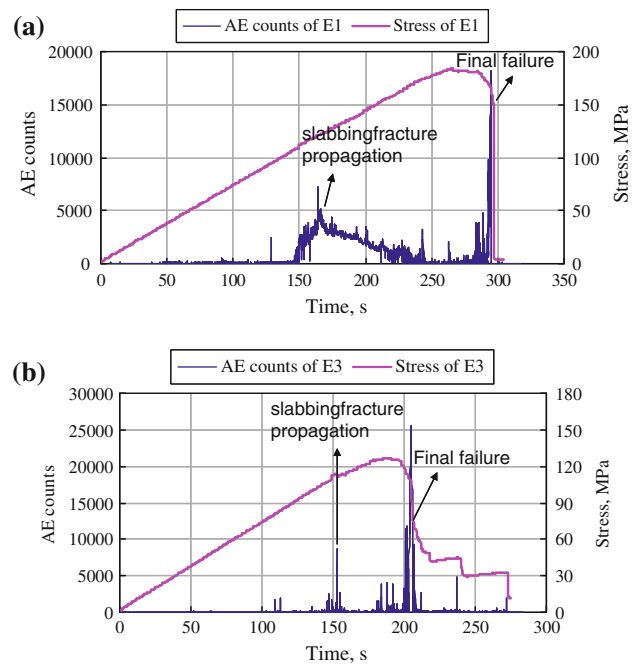
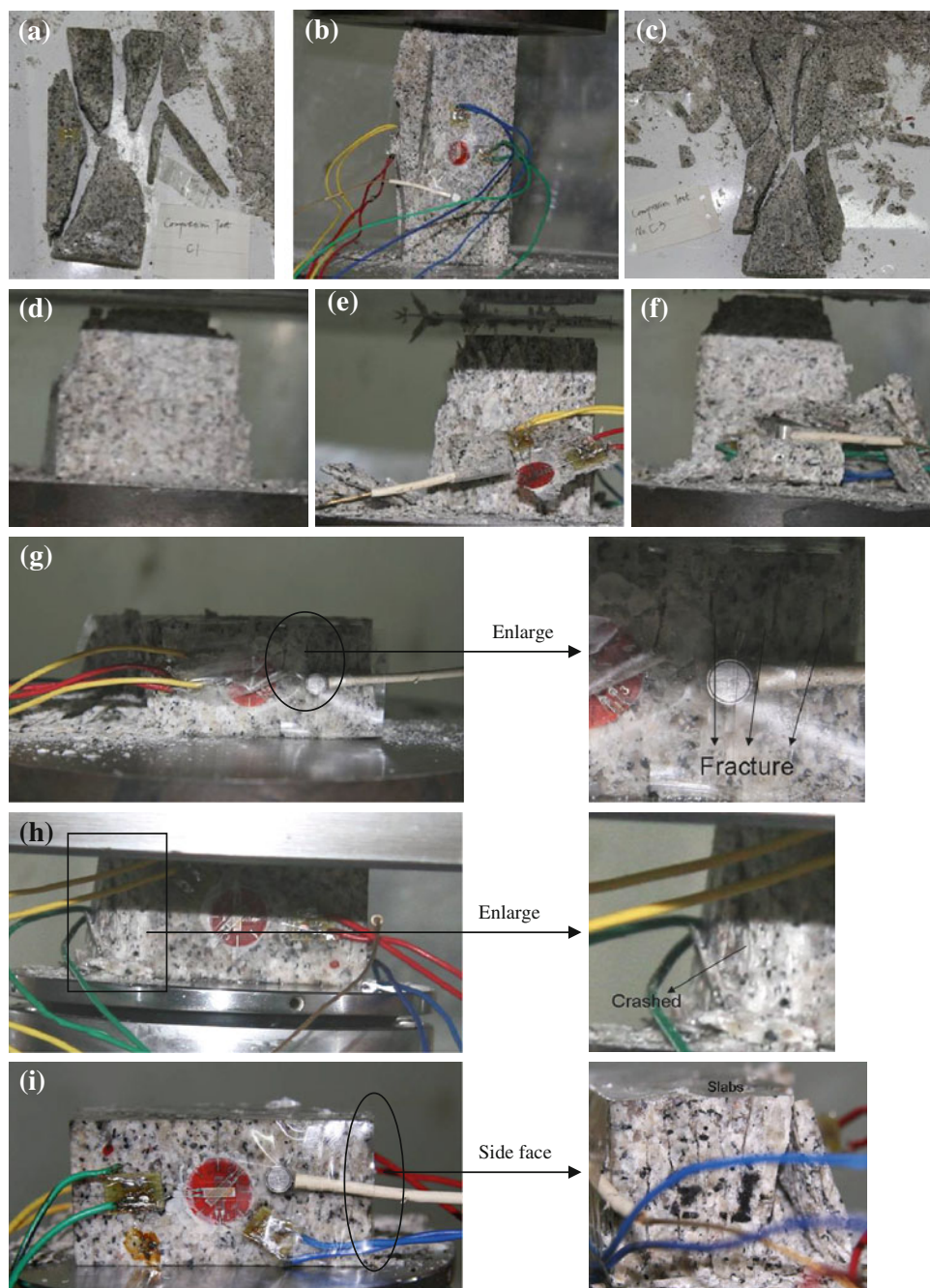


Fig. 11 The AE counts–time curve and the stress–time curve in Group E. **a** Specimen: E1, **b** specimen: E3

failure dominates the failure process in C and D specimens. The increase in UCS may be caused by the confinement of the ends in the case of D specimens. The UCS of the E specimens varies over a large range. Two of the three E specimens, E1 and E3, failed obviously in slabbing. Specimen E2 was an exception to Group E, since the failure occurred in a small portion that was ejected from the specimen. It may be the result of the stress concentration caused by mismatching between the specimen ends and the loading platens. The final failure mode of the specimens has been changed from shear at $H/W = 1$ to slabbing at $H/W = 0.5$. The drop of UCS for specimens E1 and E3 is possibly due to the change in failure mode. From the curves of specimen E1 and E3 (Figs. 10, 11), it can be seen that the AE count rate increases significantly when the stress reaches about 110 MPa and the axial strain data seems to be invalid or partially invalid afterwards. It can be inferred that when the stress reaches about 110 MPa, the slabbing fractures start to initiate and develop. Since the slabbing fractures are almost parallel to the loading direction, the specimen can still sustain further loading.

The fracture angle (θ) of a fracture plane is defined as the angle between the normal line to the fracture plane and the loading direction. The fracture angles were measured by the macro fractures of the specimens after testing. The fracture angles of all the compression specimens are plotted in Fig. 14 with respect to the ratio of height to width (H/W).

Fig. 12 Failure modes of the prism specimens in groups C, D and E. **a** Specimen: C1, **b** specimen: C2, **c** specimen: C3, **d** specimen: D1, **e** specimen: D2, **f** specimen: D3, **g** specimen: E1, **h** specimen: E2, **i** specimen: E3



The fracture angle of the prism specimens changes from about 70° to 86° when the H/W ratio decreases from 2.4 to 0.5. The shear fracture can be clearly observed in the C specimens ($H/W = 2.4$), but it is not so obvious in the D specimens ($H/W = 1.0$). The failure mode of the D specimens might be a mixture of shear and slabbing as the result of end effects. The fractures in the shortest specimens ($H/W = 0.5$) are approximately parallel to the loading direction and almost equal-spaced distributed in the specimens.

3.2 Relationship Between Stress, Strain and AE Counts

On the stress–strain and AE count rate curves of the long specimens (Groups A and C), three critical points P, Q and M are identified, as shown in Figs. 4 and 8. Point P marks the onset of the monotonically increasing AE count rate, and point Q marks the end of this process. Microcracking initiates and propagates in a stable manner between P and Q. Microcracks begin to coalesce at point Q and propagate in an unstable manner afterward. The stress at P is denoted

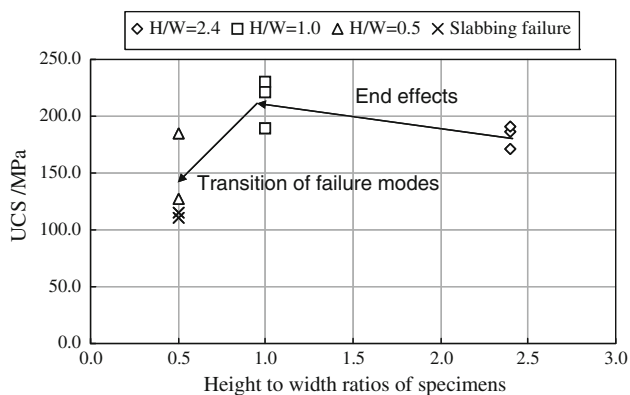


Fig. 13 The variation of the UCS with the height/width ratio for the three groups of prism specimens

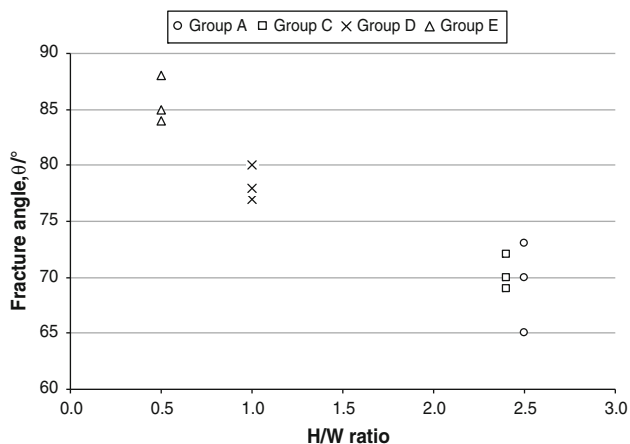


Fig. 14 The variation of the fracture angle with the height/width ratio for the specimens under uniaxial compression

as σ_{st} (stable crack initiation stress) and the stress at Q is denoted as σ_{ust} (unstable crack development stress). Point M is determined on the stress–lateral strain curve where the lateral strain departs from its linearity. The stress at M is denoted as σ_{sl} (slabbing stress).

Since we define the ‘M’ threshold as being the lateral strain that departs from its linearity, we can use the secant lateral stiffness as a parameter to determine the ‘M’ threshold where the lateral stiffness also departs from its linearity. In our analysis, we can obtain the lateral stiffness of specimens by using the stress divided by the lateral strain. These three stress levels can be obtained in Figs. 4 and 8. The value of σ_{st} , σ_{ust} and σ_{sl} for the specimens in Groups A and C are listed in Table 3. The percentages of σ_{st} , σ_{ust} and σ_{sl} to the uniaxial compressive strength are also listed in Table 3. It is seen that they are about 30, 90 and 60% of the UCS, respectively. It is observed that the lateral strain at point M ranges from 420 to 700 $\mu\epsilon$ and has an average value of 550 $\mu\epsilon$. It is approximately equal to the

maximum extension strain of the rock obtained from the Brazilian disc tests.

Martin and Chandler (1994) and Eberhardt et al. (1998) have put forward some stress thresholds for the crack closure (σ_{cc}), crack initiation (σ_{ci}) and crack damage (σ_{cd}) of hard rock in uniaxial compression tests. The comparisons between our methods and theirs are listed here to show the difference between these thresholds. Martin (1993) suggested one to use calculated crack volumetric strain to identify crack initiation. For a uniaxially loaded sample, crack volume is determined by subtracting the linear elastic component of the volumetric strain, given by:

$$\epsilon_{Velastic} = \frac{1 - 2\nu}{E} \sigma_{axial} \tag{1}$$

where E and ν are the elastic constants, from the volumetric strain calculated from the measured axial and lateral strain, given by:

$$\epsilon_V = \epsilon_{axial} + 2 \cdot \epsilon_{lateral} \tag{2}$$

The remaining volumetric strain is attributed to axial cracking, i.e.,

$$\epsilon_{Vcrack} = \epsilon_V - \epsilon_{Velastic} \tag{3}$$

Therefore, the volumetric strain and the calculated crack volumetric strain can be plotted with applied stress in the stress–strain curves. Martin (1993) defines crack initiation as the stress level at which dilation (i.e., crack volume increase) begins in the crack volume plot. Taking the typical cylindrical specimen A3 and rectangular prism specimen C3 as examples, the stress–strain curves, the AE count rate curve and the stress thresholds are plotted in Figs. 15 and 16, respectively.

In the Figs. 15 and 16, five curves are shown to determine the stress thresholds at the six points. For example, the thresholds of σ_{cc} , σ_{ci} , and σ_{cd} are determined by the calculated crack volumetric strain curve and the volumetric strain curve by Martin’s method. The thresholds of σ_{st} , and σ_{ust} are determined by the AE count rate curve where the AE counts increase monotonically. The threshold of σ_{sl} is determined by the lateral strain curve where it departs from its linearity. It can be seen that these thresholds have some difference in the two figures. The relationship of these thresholds can be described by the following inequality:

$$\sigma_{cc} < \sigma_{st} < \sigma_{ci} < \sigma_{sl} < \sigma_{cd} < \sigma_{ust} < \sigma_{ucs} \tag{4}$$

where σ_{ucs} is the uniaxial compressive strength.

In the studies of Eberhardt et al. (1998) and Diederichs et al. (2004), the traditional strain measurement method has been used to determine the damage threshold as σ_{cc} , σ_{ci} and σ_{cd} . Meanwhile, these authors have also used the AE measurement result as an important parameter to identify these thresholds. According to the study of Eberhardt et al. (1998),

Table 3 Data from the critical points on the stress–strain curves of the A and C specimens

Specimen number	Point P			Point Q			Point M			UCS
	ϵ_{axial} ($\mu\epsilon$)	σ_{st} (MPa)	σ_{st}/σ_c (%)	ϵ_{axial} ($\mu\epsilon$)	σ_{ust} (MPa)	σ_{ust}/σ_c (%)	$\epsilon_{lateral}$ ($\mu\epsilon$)	σ_{sl} (MPa)	σ_{sl}/σ_c (%)	
A1	1,400	70	36	3,280	180	91	550	130	66	197
A2	1,100	50	23	3,100	175	81	700	130	60	215
A3	1,200	52	26	3,550	188	95	460	128	65	198
C1	900	48	28	2,600	148	87	420	105	61	171
C2	1,000	50	27	3,050	160	86	620	115	61	187
C3	1,150	55	29	3,400	176	92	550	120	63	191
Average	1,142	55	29	3,163	171	89	550	121	63	193

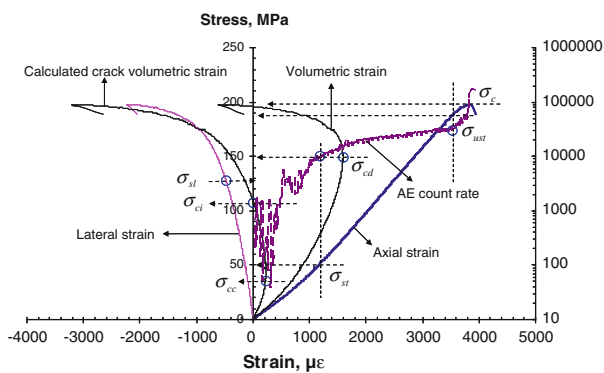


Fig. 15 Determination of stress damage thresholds by Martin’s method and ours for the typical cylindrical specimen A3

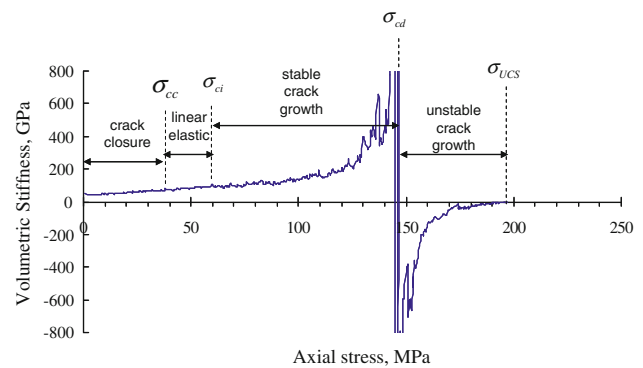


Fig. 17 Determination of the stress damage thresholds by volumetric stiffness with Eberhardt’s method in the compressive failure process of specimen A3

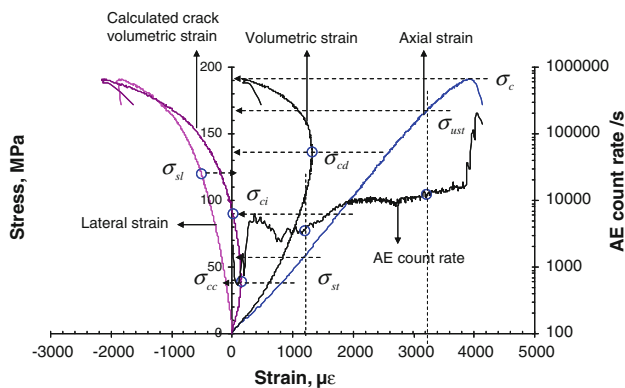


Fig. 16 Determination of stress damage thresholds by Martin’s method and ours for the typical rectangular prism specimen C3

the damage thresholds of σ_{ci} and σ_{cd} were basically determined by the volumetric stiffness and then validated through acoustic emission analysis. If we use this method on the specimen A3 in our tests, the volumetric stiffness versus the applied stress can be obtained and shown in Fig. 17. The damage thresholds can be derived from Fig. 17, where $\sigma_{cc} = 38$ MPa, $\sigma_{ci} = 60$ MPa and $\sigma_{cd} = 146$ MPa. Then the AE event counts, duration and ring down counts versus the axial stress can be drawn to help find out these damage

thresholds. Therefore, the acoustic emission measurement is an additional tool for determining these damage thresholds by Eberhardt et al. (1998). It can be seen that the inequality: $\sigma_{cc} < \sigma_{st} < \sigma_{ci} < \sigma_{sl} < \sigma_{cd} < \sigma_{ust} < \sigma_{UCS}$ is still qualified by this method. Note that the damage threshold of σ_{ci} becomes less than the value obtained by Martin’s method, and it is almost equal to the value of σ_{st} by our method.

However, some of these damage thresholds are difficult to obtain in the short specimens such as in Group D and E. For example, the critical point M (the threshold of σ_{sl}) did not appear on the stress–strain curves of D specimens ($H/W = 1.0$). It seems that the lateral extension strain is almost linear prior to failure. The UCS of D specimens is higher than the UCS of C specimens. This may be due to the end effects in the specimens. The strength of the shortest specimens in group E ($H/W = 0.5$) is not as high as expected, from the view point of the end effects. For example, two of the three specimens have low uniaxial compression strength (specimens E1 and E3). The strength of E1 is about 184 MPa, but at the stress level of 115 MPa the AE count rate has an abrupt jump (Figs. 10a, 11a). It probably means that at this stress level, the slabbing fractures begin to develop in the specimen. The same

phenomenon also took place on specimen E3 as shown in Figs. 10c and 11b.

3.3 Failure Mode and the Slabbing Strength of Hard Rock

In this study, slabbing failure was observed in the shortest specimens (group E). The failure modes in the prismatic specimens are sketched in Fig. 18. On the one hand, slabbing fractures can be formed in short prismatic specimens under uniaxial compression. Slabs are created parallel to the direction of the maximum compressive load. On the other hand, by carefully observing the shear fractures in the long specimens, it was found that a great number of microfractures parallel to the loading direction existed in the specimens. Since the specimens are long, the microfractures cannot penetrate the samples to form thin slabs easily toward the center of the sample, but finally coalesce together and form a shear band. It means that the fractures will propagate parallel with the loading direction and, finally, form slabbing fractures in short specimens, but will end up as shear fractures in long specimens.

When slabbing failure occurs, the corresponding stress is defined as the slabbing strength of the rock. According to the laboratory study, the slabbing-failed specimens E1 and E3 have lower strengths than C and D specimens. The slabbing strength of Iddefjord granite is about 120 MPa. This value is approximately equal to the stress level when the lateral strain departs from its linearity for the long specimens. The slabbing strength of the Iddefjord granite is about 60% of its UCS value for standard specimens.

The observations of the Atomic Energy of Canada Limited (AECL's) Mine-by Experiment support the above claim on the slabbing strength of hard rock (Martin 1997). It was observed in the Mine-by Experiment that the brittle spalling failure initiated when the maximum tangential stress on the boundary of the tunnel reached 120 MPa. The mean uniaxial compressive strength of Lac du Bonnet granite was 212 MPa. The onset of brittle failure (spalling or slabbing) occurred, therefore, at a stress level of $120/212 = 0.56$ UCS. This 120 MPa value was also confirmed by Read (2004), by excavating tunnels with various

shapes and various orientations relative to the in situ stress state at the 420 Level in the experiment mine. It was reported that the in situ stress magnitudes were $\sigma_1 = 60 \pm 3$, $\sigma_2 = 45 \pm 4$ and $\sigma_3 = 11 \pm 2$ MPa at the 420 Level. The in situ stresses are very high and after tunnel excavation the stress concentrations around the tunnel will lead to approximately uniaxial compression on the boundary of the underground excavation. The loading conditions are similar to the laboratory tests; then the spalling or slabbing fractures begin to propagate and finally form a V-shaped notch at the stress concentration place around the excavation. The stress level for creating slabbing fractures is about $(60 \pm 5)\%$ of the UCS of Lac du Bonnet granite in the site.

The induced stresses and the stress path are both related to the spalling failure of hard rock. On the one hand, when excavating a tunnel in highly stressed hard rocks, the maximum tangential stress surrounding the tunnel can be predicted by the Krusch's equation: $\sigma_{\text{tan}} = 3\sigma_1 - \sigma_3$. If the in situ stresses are very high, then the maximum tangential stress may reach the slabbing strength of the rock. On the other hand, when the tunnel is excavated, the radial stress will be near zero. It means that the stress path is changed and the stress conditions created in the surrounding rock become almost uniaxial compression. Therefore, we can conclude that if the maximum tangential stress surrounding an underground excavation reaches about 60% of UCS value of intact rock, slabbing and spalling failure may take place on the boundary of the excavation. The in situ stresses and the induced stresses play an important role in the formation of slabbing fractures in underground engineering. The best way to stop or eliminate slabbing failure is to control the excavation boundary to avoid big stress concentration, so that the maximum tangential stress could be under the slabbing threshold. Another method in underground mining engineering is to apply backfill technology, which can supply certain confining pressure on the surrounding rock to stop the growing of slabbing fractures.

4 Conclusions

By changing the sample height-to-width ratio in the uniaxial compression laboratory tests, slabbing failure is achieved in the short rectangular prismatic specimens. It is found out that the failure mode of hard rock may be transformed from shear to slabbing when the height/width ratio of the prism specimen is smaller than, for example, 0.5 under uniaxial compression. The slabbing strength of hard rock is about 60% of the UCS of the rock. Slabbing fractures are approximately parallel to the loading direction, so that the slabs of hard rock can still sustain some further loading. The initiation and propagation of slabbing fractures under uniaxial compression may occur when the

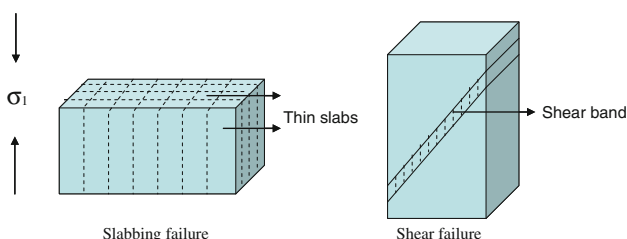


Fig. 18 The failure modes of rectangular prism specimens of hard rock

lateral extension strain reaches about the maximum extension strain obtained from the Brazilian disc test.

For long specimens, such as groups A and C, the lateral strain will depart from its linearity at this critical point. The stress thresholds of σ_{st} , σ_{ust} and σ_{sl} are compared with the thresholds of σ_{cc} , σ_{cd} and σ_{ci} in the long specimens. It is found that the relationship between them can be described by the inequality as: $\sigma_{cc} < \sigma_{st} < \sigma_{ci} < \sigma_{sl} < \sigma_{cd} < \sigma_{ust} < \sigma_{ucs}$.

The in situ stresses and the induced stresses play an important role in the formation of slabbing fractures in underground engineering. If the maximum tangential stress surrounding an underground excavation reaches about the slabbing threshold (about 60% of UCS value of intact rock), slabbing and spalling failure may take place on the boundary of the excavation. The best way to stop or eliminate slabbing failure is to control the excavation boundary to decrease the stress concentration. Another way in mining engineering is to use backfilling technology, which can supply certain confining pressure on the surrounding rock to stop the growing of slabbing fractures.

Acknowledgments The research presented in this paper was jointly supported by the 973 Program of China (grant No. 2010CB732004), the Natural Science Foundation of China (grant No. 50934006 and 10872218) and the Norwegian Research Council (grant no. 10330422). The first author would like to thank the Chinese Scholarship Council for financial support to the joint PhD study at NTNU, Norway. The authors would like to thank Arild Monsøy at NTNU, Norway, Trond Larsen at SINTEF, Norway, Professor Feng Chen and Dr. Chunde Ma at Central South University, China, for their assistance in the preparation of the specimens and the laboratory testing. Also, the authors express their acknowledgements to the anonymous reviewers for their precious comments.

Open Access This article is distributed under the terms of the Creative Commons Attribution Noncommercial License which permits any noncommercial use, distribution, and reproduction in any medium, provided the original author(s) and source are credited.

References

- Bazant ZP, Xiang Y (1996) Compression failure in reinforced concrete columns and size effect, Structures Congress—Proceedings, pp 443–451
- Bazant ZP, Xiang Y (1997) Size effect in compression fracture: splitting crack band propagation. *J Eng Mech* 123:162–172
- Bazant ZP, Kim JH, Daniel IM, Becq-Giraudon E, Zi G (1999) Size effect on compression strength of fiber composites failing by kink band propagation. *Int J Fract* 95:103–141
- Bieniawski ZT (1967a) Mechanism of brittle fracture of rock. Part I. Theory of the fracture process. *Int J Rock Mech Min Sci* 4:395–406
- Bieniawski ZT (1967b) Mechanism of brittle fracture of rock. Part II. Experimental studies. *Int J Rock Mech Min Sci* 4:407–423
- Bieniawski ZT (1967c) Mechanism of brittle fracture of rock. Part III. Fracture in tension and under long-term loading. *Int J Rock Mech Min Sci* 4:425–430
- Brady BHG, Brown ET (2004) Rock mechanics for underground mining. Kluwer, Dordrecht
- Cai M (2008) Influence of intermediate principal stress on rock fracturing and strength near excavation boundaries—insight from numerical modeling. *Int J Rock Mech Min Sci* 45:763–772
- Chunlin Li (1995) Micromechanics modelling for stress–strain behaviour of brittle rocks. *Int J Numer Anal Methods Geomech* 19:331–344
- Cook NGW (1965) The failure of rock. *Int J Rock Mech Min Sci* 2:389–403
- Diederichs MS (2002) Stress induced damage accumulation and implications for hard rock engineering. In: Hammah R, Bawden W, Curran J, Telesnicki M (eds) Mining and tunnelling innovation and opportunity. Proceedings of the 5th North American Rock Mechanism Symposium and the 17th Tunnelling Association of the Canada Conference, Toronto 1:3–12. Univ. Toronto Press, Toronto
- Diederichs MS (2007) The 2003 Canadian Geotechnical Colloquium: Mechanistic interpretation and practical application of damage and spalling prediction criteria for deep tunnelling. *Can Geotech J* 44:1082–1116
- Diederichs MS, Kaiser PK, Eberhardt E (2004) Damage initiation and propagation in hard rock during tunnelling and the influence of near-face stress rotation. *Int J Rock Mech Min Sci* 41:785–812
- Dowding CH, Andersson CA (1986) Potential for rock bursting and slabbing in deep caverns. *Eng Geol* 22:265–279
- Eberhardt E (1998) Brittle rock fracture and progressive damage in uniaxial compression, Ph.D. thesis, Department of Geological Sciences. University of Saskatchewan, Saskatoon, Canada, p 334
- Eberhardt E, Stead D, Stimpson B, Read RS (1998) Identifying crack initiation and propagation thresholds in brittle rock. *Can Geotech J* 35:222–233
- Eberhardt E, Stead D, Stimpson B (1999) Quantifying progressive pre-peak brittle fracture damage in rock during uniaxial compression. *Int J Rock Mech Min Sci* 36:361–380
- Ewy RT, Cook NGW (1990a) Deformation and fracture around cylindrical openings in rock. I. Observations and analysis of deformations. *Int J Rock Mech Min Sci* 27:387–407
- Ewy RT, Cook NGW (1990b) Deformation and fracture around cylindrical openings in rock-II. Initiation, growth and interaction of fractures. *Int J Rock Mech Min Sci Geomech Abstr* 27:409–427
- Exadaktylos GE, Tsoutrelis CE (1995) Pillar failure by axial splitting in brittle rocks. *Int J Rock Mech Min Sci Geomech Abstr* 32:551–562
- Fairhurst C, Cook NGW (1966) The phenomenon of rock splitting parallel to the direction of maximum compression in the neighborhood of a surface. In: Proceedings of the First Congress on the International Society of Rock Mechanics, Lisbon, pp 687–692
- Fang Z, Harrison JP (2002) Development of a local degradation approach to the modelling of brittle fracture in heterogeneous rocks. *Int J Rock Mech Min Sci* 39:443–457
- Germanovich LN, Dyskin AV (2000) Fracture mechanisms and instability of openings in compression. *Int J Rock Mech Min Sci* 37:263–284
- Hajiabdolmajid V, Kaiser PK, Martin CD (2002) Modelling brittle failure of rock. *Int J Rock Mech Min Sci* 39:731–741
- Holzhausen GR, Johnson AM (1979) Analyses of longitudinal splitting of uniaxially compressed rock cylinders. *Int J Rock Mech Min Sci Geomech Abstr* 16:163–177
- Horii H, Nemat-Nasser S (1986) Brittle failure in compression: splitting, faulting and brittle–ductile transition. *Philos Trans R Soc Lond (Math Phys Sci)* 319:337–374
- Kaiser PK, McCreath DR (1994) Rock mechanics considerations for drilled or bored excavations in hard rock. *Tunn Undergr Space Technol Incorporat Trench* 9:425–437

- Li C, Nordlund E (1993) Deformation of brittle rocks under compression-with particular reference to microcracks. *Mech Mater* 15:223–239
- Lockner DA, Byerlee JD, Kuksenko V, Ponomarev A, Sidorin A (1991) Quasi-static fault growth and shear fracture energy in granite. *Nature* 350:39–42
- Martin CD (1993) Strength of Massive Lac du Bonnet Granite around underground openings, Ph.D. thesis, Department of Civil and Geological Engineering, University of Manitoba, Winnipeg
- Martin CD (1997) Seventeenth Canadian geotechnical colloquium: the effect of cohesion loss and stress path on brittle rock strength. *Can Geotech J (Revue Canadienne de Geotechnique)* 34:698–725
- Martin CD, Chandler NA (1994) Progressive fracture of Lac du Bonnet granite. *Int J Rock Mech Min Sci* 31:643–659
- Martin CD, Maybee WG (2000) The strength of hard-rock pillars. *Int J Rock Mech Min Sci* 37:1239–1246
- Martin CD, Read RS, Martino JB (1997) Observations of brittle failure around a circular test tunnel. *Int J Rock Mech Min Sci Geomech Abstr* 34:1065–1073
- Mogi K (2007) *Experimental rock mechanics*. Taylor & Francis, London
- Moore DE, Lockner DA (1995) Role of microcracking in shear-fracture propagation in granite. *J Struct Geol* 17:95–114
- Ortlepp WD (1997) Rock fracture and rockbursts: an illustrative study. South African Institute of Mining and Metallurgy, Johannesburg
- Ortlepp WD (2001) The behaviour of tunnels at great depth under large static and dynamic pressures. *Tunn Undergr Space Technol* 16:41–48
- Ortlepp WD, Stacey TR (1994) Rockburst mechanisms in tunnels and shafts. *Tunn Undergr Space Technol* 9:59–65
- Read RS (2004) 20 years of excavation response studies at AECL's underground research laboratory. *Int J Rock Mech Min Sci* 41:1251–1275
- Savage JC, Lockner DA, Byerlee JD (1996) Failure in laboratory fault models in triaxial tests. *J Geophys Res* 101:22215–22224
- Seah CC (2006) Penetration and perforation of granite targets by hard projectiles. Ph.D. thesis, The Norwegian University of Science and Technology, Trondheim, Norway
- Stacey TR (1981) A simple extension strain criterion for fracture of brittle rock. *Int J Rock Mech Min Sci* 18:469–474
- Wong RHC, Lin P, Tang CA (2006) Experimental and numerical study on splitting failure of brittle solids containing single pore under uniaxial compression. *Mech Mater* 38:142–159